

Research Article

B-Doped Si@C Nanorod Anodes for High-Performance Lithium-Ion Batteries

Shibin Liu,¹ Jianwei Xu,¹ Hongyu Zhou,¹ Jing Wang ,² and Xiangcai Meng ¹

¹School of Materials Science and Engineering, Jiamusi University, Jiamusi 154007, China

²School of Materials Science and Engineering, Baise University, Baise 533000, China

Correspondence should be addressed to Jing Wang; jmsdxwangjing123@163.com and Xiangcai Meng; 365383263@qq.com

Received 26 September 2019; Revised 8 December 2019; Accepted 10 December 2019; Published 30 December 2019

Academic Editor: David Cornu

Copyright © 2019 Shibin Liu et al. This is an open access article distributed under the Creative Commons Attribution License, which permits unrestricted use, distribution, and reproduction in any medium, provided the original work is properly cited.

B doping plays an important role in improving the conductivity and electrochemical properties of Si anodes for Li-ion batteries. Herein, we developed a facile and massive production strategy to fabricate C-coated B-doped Si (B-Si@C) nanorod anodes using casting intermediate alloys of Al-Si and Al-B and dealloying followed by C coating. The B-Si@C nanorod anodes demonstrate a high specific capacity of 560 mAg^{-1} , with a high initial coulombic efficiency of 90.6% and substantial cycling stability. Notably, the melting cast approach is facile, simple, and applicable to doping treatments, opening new possibilities for the development of low-cost, environmentally benign, and high-performance Li-ion batteries.

1. Introduction

The increasing requirement for large-scale energy storage devices has triggered the development of high-energy density Li-ion batteries (LIBs) [1–5]. Among various anode materials, Si has been regarded as a promising candidate because of its superior theoretical specific capacity of 4200 mAhg^{-1} [6] and appropriate charging potential (0.4 V vs. Li^+/Li) [7]. However, the practical application of Si anodes suffers from a severe challenge because of poor cyclic stability arising from their huge volume change (greater than 300%) and low conductivity. In addition, their low initial coulombic efficiency has also impeded the development of practically viable Si anodes [8].

In view of the aforementioned problems with Si, the synthesis of nanostructured Si, such as nanoparticles, nanowires, nanotubes, and nanosheets, is a feasible strategy to alleviate the detrimental effects of Si volume expansion and improve long-term cycle stability [9–11]. Nanostructured Si can effectively shorten the transmission path of electrons and lithium ions [12]. Although these studies have achieved good results, improvements in the conductivity of Si remain limited because of the semiconductor properties of Si itself. At the same time, the preparation of nanostructured Si often requires rigorous experimental conditions such as high vac-

uum, high temperatures, high pressures, and even highly toxic reaction materials. In addition, low product yields make industrialized production difficult [13, 14]. These conditions limit the further application of nanostructured Si materials in LIBs.

Element doping is an effective way to improve the conductivity of Si materials. Yi et al. [15] successfully prepared boron-doped porous Si by adding B_2O_3 to a SiO thermal disproportionation reaction. Boron doping can effectively improve the microcapacity of Si-C composites at high current densities. The results show that B-doped Si-C composites exhibit better rate performance than undoped Si-C composites. Chen et al. [16] prepared B-doped porous Si nanoplates with high crystallinity via an air oxidation degaussing method using p-type Si wafers as raw materials. Compared with the original material, the B-doped material exhibited greatly improved conductivity. The Si material has excellent cycling performance and high initial coulombic efficiency. Our previous work has shown that a large number of defects formed during synthesis of Si nanorods are conducive to the earlier occurrence of stress relaxation from brittle Si to plastic $\text{Li} \times \text{Si}$ [17]; accordingly, defects such as dislocations, twists, and stacking faults can effectively improve the cycle life of Si nanorods. Bindumadhavan et al. [18] studied

B-doped reduced graphene as an anode material for LIBs. They found that B doping was related to the formation of a large number of defects in the matrix. Therefore, B doping treatment increased not only the electron density but also the defect number, which is favourable for increasing the electron transfer rate [19] and improving the cyclic stability of Si anodes arising from a stress release induced by defect accumulation [20].

At present, the most common B doping methods are oxidation-reduction and solid-state sintering methods, both of which demand harsh reaction conditions and are unsuitable for massive production, hindering further development of Si as an anode material for LIBs [21–23].

With the exception of B doping, carbon coatings not only improve conductivity but also stabilize the structure of Si. Gao et al. [24] prepared a Si@C composite anode material with a core-shell structure using PZS as a pyrolyzed carbon source. The results show that the material has a stable structure and improves the cyclic stability and conductivity of Si anode materials.

Herein, we propose fabricating a C-coated B-doped Si (denoted as B-Si@C) nanorod composite using casting intermediate alloys of Al-Si and Al-B and dealloying Al followed by C coating using polydopamine as a carbon source. Compared with the traditional Si anode material, the B-Si@C anode displays an initial coulombic efficiency as high as 90.6% and maintains a capacity of 560 mAhg⁻¹ at 1000 mA g⁻¹ for 500 cycles as well as good rate capability. These promising results suggest that B doping in Si by melt casting is a successful method for large-scale production of element-doped nanostructured Si materials, which can effectively improve the comprehensive electrochemical properties of Si anodes and potentially be commercialized for high-performance Li-ion batteries.

2. Experimental

2.1. Material Preparation and Structure Characterization. B_{0.5}-Al-Si₁₃ ingots were first prepared by casting Al-Si and Al-B intermediate alloys in a medium-frequency induction furnace at 720–780°C followed by rapid solidification. After acid etching the Al in the ingots and filtering, the obtained B-doped Si was C coated using as anode materials for LIBs. The alloys used in this study were purchased from Xuzhou Huayang Aluminum Co., Ltd. Dopamine was used as a carbon source, and Tris was used as a buffer to prepare a layer of C on the surface of the B-doped nanosilicon anode material. A total of 0.5 g of B-doped Si was added to 10 M Tris buffer (200 ml, adjusted pH = 8.5). After ultrasonic dispersal for 30 min, 0.5 g of dopamine was added, and the solution was ultrasonically dispersed for an additional 20 min. The mixed solution was stirred for 24 h under aerobic conditions to self-polymerize. The obtained mixture was filtered and washed with deionized water several times. B-Si@PDA was subsequently obtained by vacuum drying the mixture at 70°C. Finally, the obtained B-Si@PDA was placed into an empty drying oven and the temperature was increased at a rate of 5°C min⁻¹ to 800°C and maintained at this temperature for 2 h to obtain B-Si@C.

2.2. Material Characterization. The morphology of the B-Si@C composite materials was characterized by scanning electron microscopy (SEM, S4800, Hitachi, Japan) and transmission electron microscopy (TEM, Jeol 2100F). Wide-angle X-ray powder diffraction (XRD) patterns were collected on an X-ray diffractometer (Ultima IV, Japan) equipped with a Cu anode ($V = 40$ kV, $I = 20$ mA) at a scanning rate of 5°/s in reflection mode over the 2θ range from 10° to 90°. Raman spectra were recorded on a micro-Raman system (LabRam HR Evolution, France), and X-ray photoelectron spectroscopy (XPS) analysis was carried out on a Thermo Scientific K-Alpha photoelectron spectrometer equipped with monochromatic Al K α X-ray source.

2.3. Electrochemical Performance Tests. The prepared B-Si@C was mixed with graphite and acetylene black in a certain proportion to prepare the anode active material, and sodium alginate was used as a binder to evenly grind and mix the powders. The ground powder was evenly coated onto copper foil, and the coating amount was approximately 0.9–1.9 mg. The copper foil was placed in an 80°C vacuum drying box for 24 h and then pressed into sheets. LiPF₆, ethylene carbonate (EC), diethyl carbonate (DEC), and dimethyl carbonate (DMC) were mixed proportionally as the electrolyte, and Celgard 2400 was used as the separator. A lithium sheet served as the opposite electrode. A button battery was assembled in a glove box filled with Ar gas and was tested at room temperature after 24 h. The voltage range of the anode charge/discharge was 0.01–1.5 V; the current density of the first four cycles was 100 mA g⁻¹ and during later long-term cycling was 1000 mA g⁻¹.

3. Results and Discussion

3.1. Structure and Properties of the Materials. The XRD patterns of the B-doped Al-Si₁₃ eutectic alloy, B-free Al-Si₁₃ eutectic alloy, B-Si@C, and Si@C are shown in Figure 1. All of the XRD peaks of the eutectic Al-Si ingots can be well indexed to those of Si (JCPDS No. 77-2111) and Al (JCPDS No. 85-1327) (Figures 1(a) and 1(b)). No other peaks are observed, which implies that only Al and Si phases exist in the Al-Si ingots. The inset figure shows an enlarged view of the (111) peak. This peak shifts to a lower angle because of B doping. According to Bragg's law,

$$n\lambda = 2d \sin \theta \quad n\lambda = 2d \sin \theta. \quad (1)$$

The diffraction peak shifting leftward to a lower offset indicates an increase in the distance between planes, which contributes to the enhancement of the Li⁺ intercalation/deintercalation. Therefore, B doping in Si can effectively enlarge the [111] plane spacing and enhance the Li⁺ ion diffusion. B doping enables Si to obtain larger Li-ion transmission channels in the (111) direction, which increases the transmission rate of the lithium ions [25]. In addition, the peak intensity decreasing of B-Si@C samples after B doping indicates that B doping in Si produces a certain effect on the crystallinity of Si. The strong diffraction intensities and sharp peaks indicate that the ingots have high crystallinity. Compared

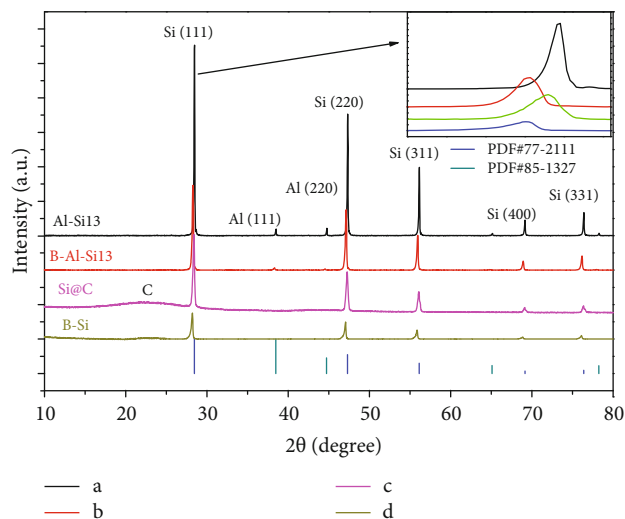


FIGURE 1: XRD patterns of B-doped Al-Si13, B-free Al-Si13, Si@C, and B-Si@C.

with the XRD diffraction patterns before and after dealloying Al (Figures 1(c) and 1(d)), the (111), (220), (311), (400), and (331) planes of Si are visible at 28.70° , 47.50° , 56.30° , 69.3° , and 78° , respectively, and the peaks of Al disappear. This result indicates a good etching effect and that Al in the alloy can be completely removed. From the XRD patterns of B-Si@C and B-Si, it is found that there are diffraction packages near 24° , corresponding to pyrolytic carbon generated after PDA being pyrolyzed and carbonized. However, this pyrolytic carbon peak is not sharp and wider, indicating that the C coated exists in the form of amorphous carbon [18].

To further confirm the presence of B in Si, we conducted XPS analysis of B-Si@C (Figure 2). Figure 2(a) shows the peak at 99.7 eV corresponding to Si^0 and the weak peak at 103.8 eV corresponding to Si^{4+} [24]. This weak peak may be due to a small amount of SiO_x formed after dealloying or exposure of fresh silicon to air. The SiO_x phase can effectively alleviate the volume effect of the active materials in the process of lithium insertion and removal [18]. As shown in Figure 2(b), the B1s peak was detected near 191.5 eV [25], which indicates that B was successfully doped into the material [16]. The content of B is 3.5% (atomic percentage) as determined by XPS, which is slightly less than the 5% composition ratio. This discrepancy likely indicates that a small amount of B is ablated during the smelting. The C peak was also detected near 285 eV (Figure 2(c)), indicating that the carbon layer was coated onto the Si surface. The carbon content was 1% (atomic percentage).

To determine the structure of the C coating, Raman spectroscopy was used to detect B-Si@C (Figure 3). The peaks at 1335 cm^{-1} and 1610 cm^{-1} correspond to the peaks of amorphous carbon (D-band) and graphitized carbon (G-band) [26], respectively. The intensity ratio between the D-band and the G-band (I_D/I_G) reflects the degree of graphitization of the carbon. The larger the I_D/I_G ratio, the lower the degree of graphitization. The I_D/I_G value in the study is 0.7, indicating that the coated carbon has a low degree of graphitization

and is close to amorphous carbon. This observation is consistent with the XRD analysis results. Compared with the standard Si single crystal peak, the Si peak shifts by 10 cm^{-1} toward lower wavenumbers, i.e., it exhibits a red shift. This shift is attributed to a decrease in the stress and strain around Si after B doping [17]. The peak intensity clearly decreases after doping with B. These results both indirectly indicate that B is present in the Si materials.

Figure 4 shows SEM micrographs of the B-Si@C material. The Si nanorods with widths of 200-400 nm are uniformly distributed. Compared with the previously reported Si [16], the morphology and size of Si differ greatly. Figure 5(a) shows TEM images of the B-doped Al-Si13 alloy. The addition of B induces a large number of very fine twins in the Al-Si eutectic alloy. The widths of these defects are very narrow, only 10-40 nm. The distribution of the twin defects is very uneven. In some regions, the twin density is high, while in others, the twin density is low or nonexistent. Figure 5(b) is a high-resolution image that shows a large number of twins in the matrix. The measured spacing of the lattice plane is 0.31 nm, which matches well with that of the (111) plane of the cubic diamond structure of Si. Defects such as dislocations and twins occur more easily on the (111) plane because of the low stacking fault energy; the stacking faults are shown in Figure 5(b) as parallel dark lines. According to the impurity-induced twinning theory proposed by Lu and Hellawell, dopant atoms can adhere to the front of the solid-liquid interface of eutectic Si, which prevents the eutectic Si from growing into blocks or flakes by a step-growth mechanism [25]. The addition of B changes the stacking order of the Si atoms and produces numerous twins in the eutectic Si, thus changing the growth direction of the eutectic Si. The selected area electron diffraction (SAED) results (Figure 5(c)) also confirm the existence of microtwin defects. Symmetrical axial twins in the (022) and (022) directions are observed. Figure 5(d) shows a TEM image of B-Si@C. The Si nanorods are 200-400 nm wide, and the C coating with a thickness of 50 nm is evenly and completely wrapped on the surfaces of the Si nanorods.

3.2. Electrochemical Performance Tests. Figure 6(a) shows the cyclic voltammetry curve of B-Si@C at a scanning rate of 0.1 mV from 0 V to 1.5 V. In the first discharge scan, the peak at 0.25 V matches the Si insertion process to form an amorphous $\text{Li} \times \text{Si}$ phase. During the first charging process, a significant peak appears at 0.55 V, which may be caused by the phase transition between $\text{Li} \times \text{Si}$ and amorphous Si [18]. In the second and subsequent cycles, a reduction peak is present at approximately 0.2 V, corresponding to the alloying of Li with amorphous Si [24]. The peak current value increases with increasing number of scans, indicating that the active material is gradually activated. The electrochemical performances of B-Si@C and Si@C in CR2032 coin batteries were compared in the range 0.01-1.5 V. The first and the 100th charging/discharging profiles based on B-doped and undoped Si@C anodes shown in Figure 6(b) indicate that the first discharge capacity of B-Si@C is 1813.8 mAhg^{-1} and that the initial coulombic efficiency is as high as 90.6%, both of these values are much higher than those of the undoped

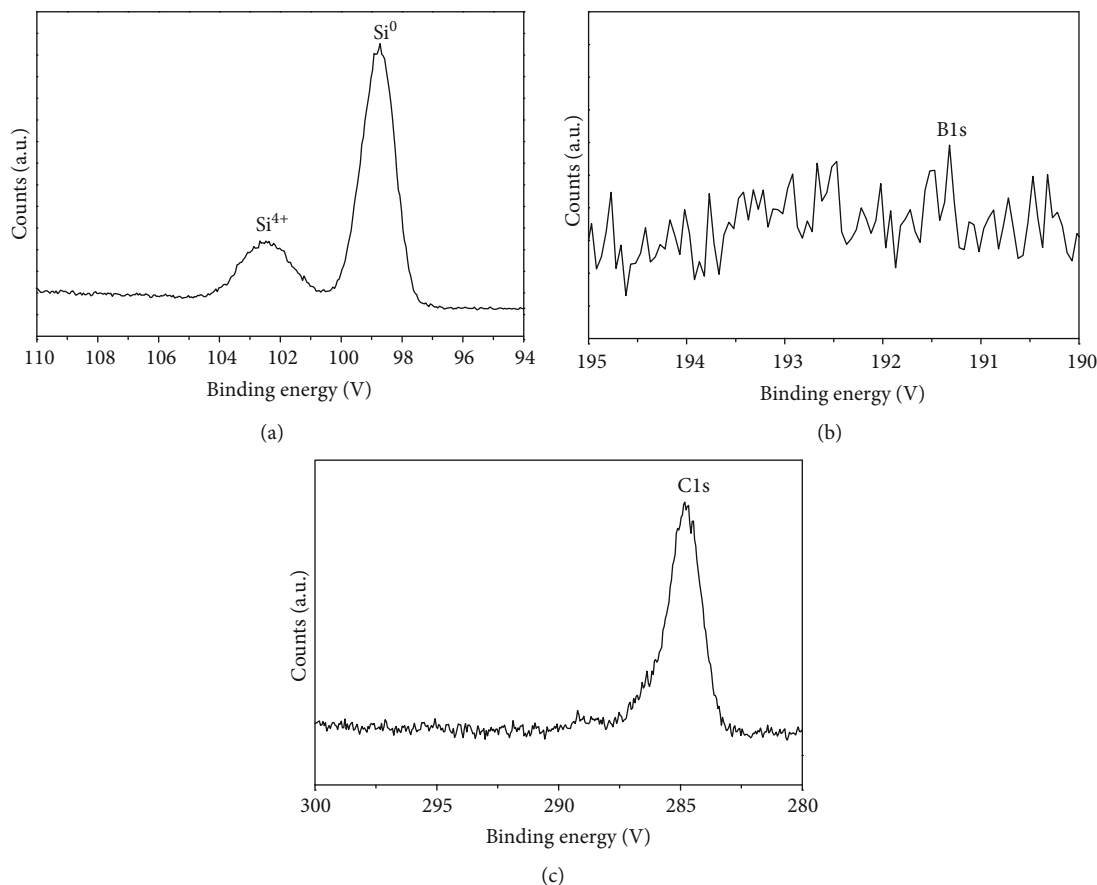


FIGURE 2: XPS of the prepared B-doped Si samples: (a) Si⁰ XPS spectra, (b) B1s XPS spectra, and (c) C1s XPS spectra.

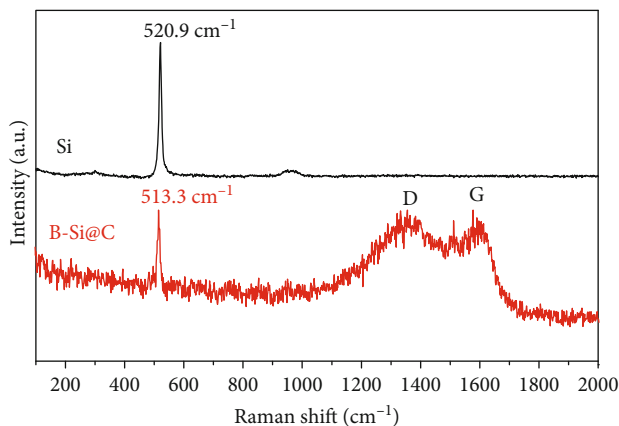


FIGURE 3: Raman spectra of samples Si and B-Si@C.

Si@C (1060.6 mAhg⁻¹ and 86.4%). In the 100th cycle, the B-Si@C anode still maintains a high reversible capacity of 680 mAhg⁻¹, indicating good reversibility of the B-Si@C anode.

We also tested the cycling stability of the B-Si@C and Si@C anodes, as shown in Figure 6(c). The current density for the first four charge-discharge cycles was 100 mA g⁻¹ and was subsequently increased to a high current density of 1000 mA g⁻¹. The cycling performances of B-Si@C, Si@C,

and Si over 500 cycles show that B-Si@C still maintains a high capacity of approximately 560 mAhg⁻¹ that is hardly attenuated from the 20th to the 500th cycle. The capacity of the Si@C anode also remains relatively stable; however, the capacity is only 320 mAhg⁻¹. The capacity of the Si anode decreases to 100 mAhg⁻¹ after 100 cycles because the Si structure is damaged during charging/discharging. In conclusion, the results show that B doping into Si can significantly improve the long-term cycling stability of Si-based electrodes at high current densities. In addition to a high first coulombic efficiency and long-term stability, the B-Si@C composites also exhibit good rate performance, as shown in Figure 6(d). The rate capability of the B-Si@C anodes was measured at different current densities from 0.1 to 4 Ag⁻¹. When the current densities are 0.1, 0.25, 0.5, 1, 2, and 4 Ag⁻¹, the discharge capacities are 2740, 2390, 1920, 1650, 840, and 460 mAhg⁻¹, respectively. When the current is restored to 0.25 Ag⁻¹, the discharge capacity also almost recovers to the original capacity (2390 mAhg⁻¹). The good cycle life and rate performance of B-Si@C are attributed to its low internal resistance.

Impedance measurements of the batteries after two cycles are shown in Figure 6(e). The AC impedance spectra of the two materials are composed of a half circle at high frequency and an oblique line at low frequency. The semicircle in the high-frequency region is related to the interface impedance and charge transfer impedance of the electrode, and the

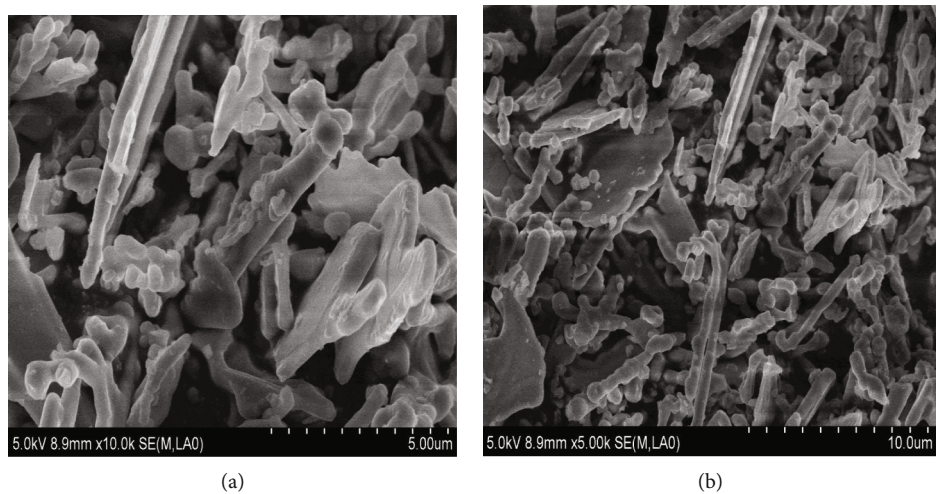


FIGURE 4: SEM image of B-Si@C.

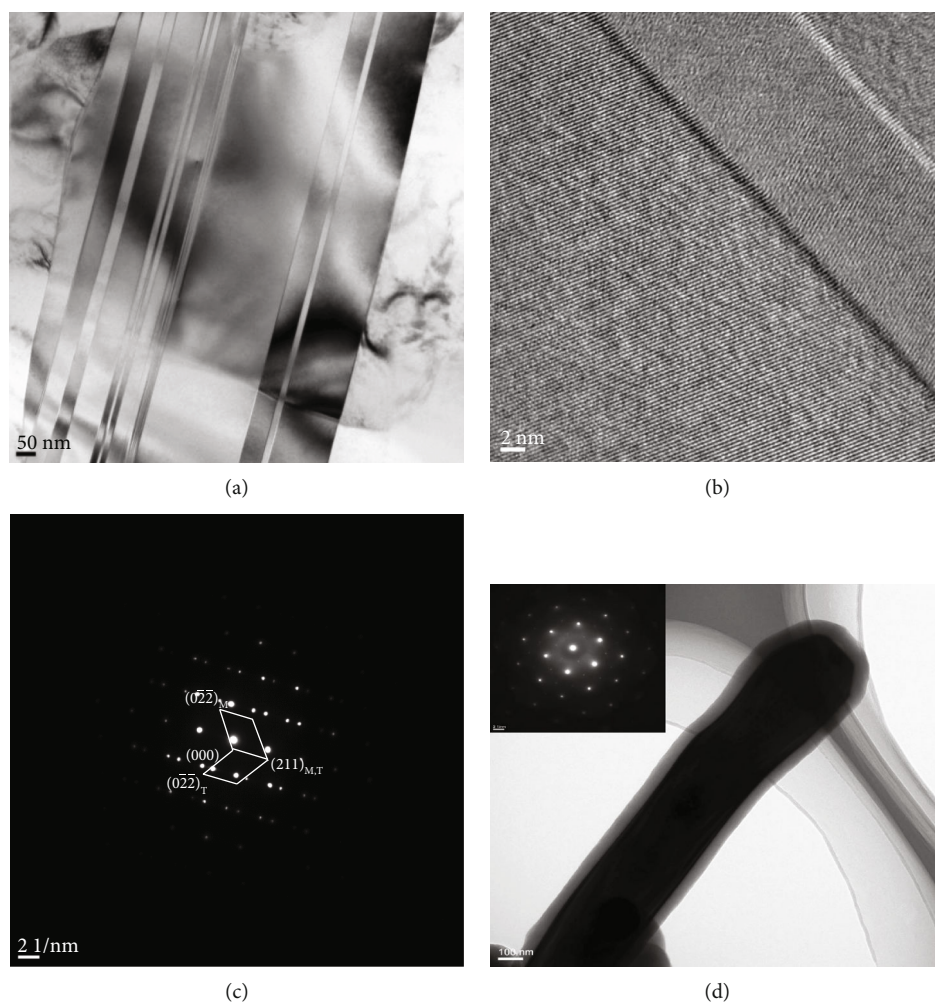


FIGURE 5: Microstructure of the B-doped Al-Si13 and B-Si@C: (a) TEM image of the B-doped Al-Si13; (b) high-resolution image of Al-Si13; (c) SAED pattern of the B-doped Al-Si13; (d) TEM image of B-Si@C.

oblique line in the low-frequency region is related to the diffusion of lithium ions in the electrode materials [27]. The B-Si@C anodes exhibit a smaller semicircle than the Si anode in

the mid-high-frequency region, which means that the conductivity of the B-Si@C anode is enhanced and its charge transfer resistance is reduced compared with those of Si.

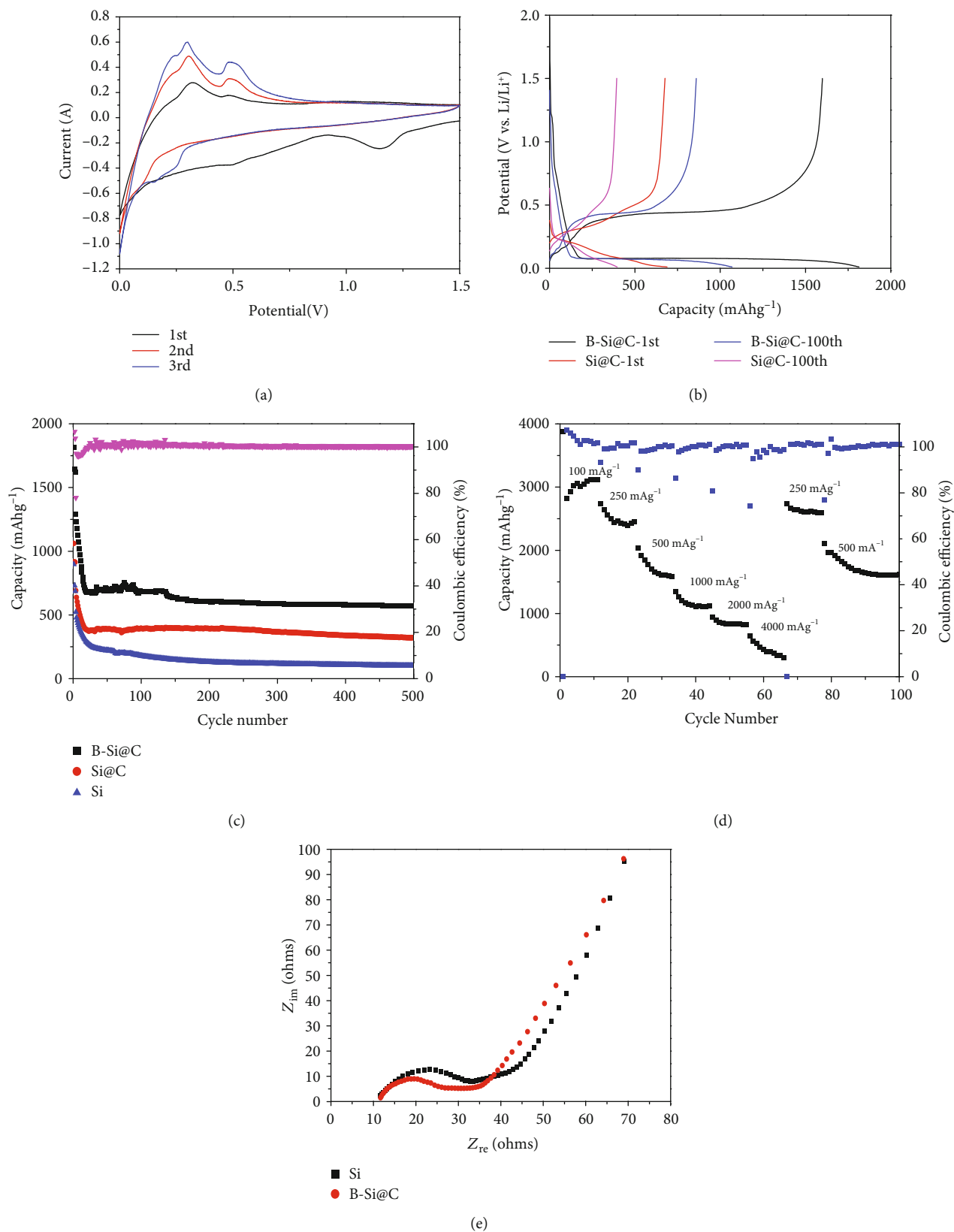


FIGURE 6: Electrochemical performances of sample: (a) volt-ampere characteristic curve; (b) discharge/charge behaviors of Si@C and B-Si@C; (c) capacity of B-Si@C, Si@C, and Si after 500 cycles; (d) rate capability behaviors of the B-Si@C composite electrode at current density from 100 to 4000 mAg⁻¹; (e) impedance spectra of B-Si@C and Si.

The steeper slope of the low-frequency line in the spectrum of B-Si@C compared with that in the spectrum of Si@C indicates that B-Si@C is in better ionic transmission state. We also compared the conductivity of B-Si@C, Si@C, and Si powders; as measured with a powder conductivity meter, the results show conductivities of $2.0 \times 10^{-4} \text{ Sm}^{-1}$ for B-Si@C, $3.4 \times 10^{-6} \text{ Sm}^{-1}$ for Si@C, and $6.7 \times 10^{-7} \text{ Sm}^{-1}$ for Si. The conductivity of the B-Si@C powder is two orders of magnitude greater than that of B-free Si@C and higher than that of Si (even three orders). These results imply that B doping and C coating both effectively improve the conductivity of Si and thus enhance its multiplier performance.

The excellent cycling stability of the B-Si@C anodes is attributed to the following factors. Firstly, the melt-cast Si surfaces with high crystallinity are resistant to oxidation, somewhat inhibiting the occurrence of electrochemical side reactions and reducing the consumption of Li^+ ions in the insertion/disinsertion process [28, 29]. Secondly, when B is doped into Si, some tetravalent Si are replaced by trivalent B to produce holes, and these holes usually generate negative charges that improve the conductivity of Si and further improve the electrochemical performance of the electrode [30–32]. Thirdly, B doping can promote the formation of abundant defects such as twins, dislocations, and faults in Si. The occurrence of these defects can release the stress accumulated during later cycling and effectively alleviate the volume expansion of the Si anode in the charge/discharge process, thereby greatly improving the cycle stability of the Si anode.

4. Conclusions

C-coated B-doped Si nanorod materials were successfully prepared from Al-Si and Al-B alloys through simple melting and casting, acid leaching of Al, followed by application of C coating. Compared with the traditional Si anode material, its conductivity is greater. The Li^+ ionic transmission rate and charge transfer are increased. In addition, the unique defect structure alleviates pulverization of Si during charging and discharging, effectively improving the cyclic stability and rate performance of Si as an anode material. The B-Si@C anodes deliver a capacity of 560 mAhg^{-1} at a current density of 1000 mA g^{-1} over 500 cycles with an initial coulombic efficiency of 90.6% as well as a good rate capability of 840 mAhg^{-1} at 2 Ag^{-1} and 460 mAhg^{-1} at 4 Ag^{-1} .

Data Availability

All data included in this study are available upon request by contact with the corresponding authors.

Conflicts of Interest

The authors declare that they have no conflicts of interest.

Acknowledgments

This work was supported by the Heilongjiang Province Natural Science Foundation (key project) (ZD2016-001),

the Fundamental Research Projects of the Fundamental Research Business Fees of the Heilongjiang Education Department (2017-KYYWF-0589), and the Graduate Science and Technology Innovation Project of Jiamusi University (LZR2015_002). The authors would like to thank C. Geng from Shiyanjia lab (<https://www.shiyanjia.com>) for SEM analysis.

References

- [1] D. Zhang, J. Wang, Y. Lin et al., “Present situation and future prospect of renewable energy in china,” *Renewable and Sustainable Energy Reviews*, vol. 76, article S1364032117303416, pp. 865–871, 2017.
- [2] A. M. Omer, “Sustainable energy development and environment,” *Research Journal of Environmental and Earth Sciences*, vol. 2, pp. 55–75, 2010.
- [3] M. Armand and J. M. Tarascon, “Building better batteries,” *Nature*, vol. 451, no. 7179, pp. 652–657, 2008.
- [4] K. Amine, R. Kanno, and Y. Tzeng, “Rechargeable lithium batteries and beyond: progress, challenges, and future directions,” *MRS Bulletin*, vol. 39, no. 5, pp. 395–401, 2014.
- [5] V. Etacheri, R. Marom, R. Elazari, G. Salitra, and D. Aurbach, “Challenges in the development of advanced Li-ion batteries: a review,” *Energy & Environmental Science*, vol. 4, no. 9, p. 3243, 2011.
- [6] J. H. Ryu, J. W. Kim, Y. E. Sung, and S. M. Oh, “Failure modes of silicon powder negative electrode in lithium secondary batteries,” *Electrochemical and Solid-State Letters*, vol. 7, no. 10, pp. A306–A309, 2004.
- [7] H. Wu and Y. Cui, “Designing nanostructured Si anodes for high energy lithium ion batteries,” *Nano Today*, vol. 7, no. 5, pp. 414–429, 2012.
- [8] B. Liang, Y. Liu, and Y. Xu, “Silicon-based materials as high capacity anodes for next generation lithium ion batteries,” *Journal of Power Sources*, vol. 267, pp. 469–490, 2014.
- [9] X. Zuo, Y. Xia, Q. Ji et al., “Self-templating construction of 3D hierarchical macro-/mesoporous silicon from 0D silica nanoparticles,” *ACS Nano*, vol. 11, no. 1, pp. 889–899, 2017.
- [10] H. Kim and J. Cho, “Superior lithium electroactive mesoporous Si@Carbon core-shell nanowires for lithium battery anode material,” *Nano Letters*, vol. 8, no. 11, pp. 3688–3691, 2008.
- [11] Z. Lu, J. Zhu, D. Sim et al., “Synthesis of ultrathin silicon nanosheets by using graphene oxide as template,” *Chemistry of Materials*, vol. 23, no. 24, pp. 5293–5295, 2011.
- [12] T. Shen, X. H. Xia, D. Xie et al., “Encapsulating silicon nanoparticles into mesoporous carbon forming pomegranate-structured microspheres as a high-performance anode for lithium ion batteries,” *Journal of Materials Chemistry A*, vol. 5, no. 22, pp. 11197–11203, 2017.
- [13] Z. Zhang, R. Zou, L. Yu, and J. Hu, “Recent research on one-dimensional silicon-based semiconductor nanomaterials: synthesis, structures, properties and applications,” *Critical Reviews in Solid State and Materials Sciences*, vol. 36, no. 3, pp. 148–173, 2011.
- [14] J. Ryu, D. Hong, S. Choi, and S. Park, “Synthesis of ultrathin silicon nanosheets from natural clays for lithium-ion battery anodes,” *ACS Nano*, vol. 10, no. 2, pp. 2843–2851, 2016.
- [15] R. Yi, J. Zai, F. Dai, M. L. Gordin, and D. Wang, “Improved rate capability of Si-C composite anodes by boron doping for

- lithium-ion batteries,” *Electrochemistry Communications*, vol. 36, pp. 29–32, 2013.
- [16] M. Chen, B. Li, X. Liu et al., “Boron-doped porous Si anode materials with high initial coulombic efficiency and long cycling stability,” *Journal of Materials Chemistry A*, vol. 6, no. 7, pp. 3022–3027, 2018.
- [17] J. Wang, X. Meng, X. Fan, W. Zhang, H. Zhang, and C. Wang, “Scalable synthesis of defect abundant Si nanorods for high-performance Li-ion battery anodes,” *ACS Nano*, vol. 9, no. 6, pp. 6576–6586, 2015.
- [18] K. Bindumadhavan, P. Y. Chang, and R. A. Doong, “Silver nanoparticles embedded boron-doped reduced graphene oxide as anode material for high performance lithium ion battery,” *Electrochimica Acta*, vol. 243, pp. 282–290, 2017.
- [19] J. Woo, S. H. Baek, J. S. Park, Y. M. Jeong, and J. H. Kim, “Improved electrochemical performance of boron-doped SiO negative electrode materials in lithium-ion batteries,” *Journal of Power Sources*, vol. 299, pp. 25–31, 2015.
- [20] N. Liu, Z. Lu, J. Zhao et al., “A pomegranate-inspired nano-scale design for large-volume-change lithium battery anodes,” *Nature Nanotechnology*, vol. 9, no. 3, pp. 187–192, 2014.
- [21] J. Wu, W. Tu, Y. Zhang et al., “Poly-dopamine coated graphite oxide/silicon composite as anode of lithium ion batteries,” *Powder Technology*, vol. 311, pp. 200–205, 2017.
- [22] Y. J. Chae, S. O. Kim, and J. K. Lee, “Employment of boron-doped carbon materials for the anode materials of lithium ion batteries,” *Journal of Alloys and Compounds*, vol. 582, pp. 420–427, 2014.
- [23] D. Uzun, “Boron-doped $\text{Li}_{1.2}\text{Mn}_{0.6}\text{Ni}_{0.2}\text{O}_2$ as a cathode active material for lithium ion battery,” *Solid State Ionics*, vol. 281, pp. 73–81, 2015.
- [24] P. Gao, J. Fu, J. Yang et al., “Microporous carbon coated silicon core/shell nanocomposite via in situ polymerization for advanced Li-ion battery anode material,” *Physical Chemistry Chemical Physics*, vol. 11, no. 47, pp. 11101–11105, 2009.
- [25] S. Z. Lu and A. Hellawell, “The mechanism of silicon modification in aluminum-silicon alloys: impurity induced twinning,” *Metallurgical Transactions A*, vol. 18, no. 10, pp. 1721–1733, 1987.
- [26] X. J. Hao, E. C. Cho, C. Flynn, Y. S. Shen, G. Conibeer, and M. A. Green, “Effects of boron doping on the structural and optical properties of silicon nanocrystals in a silicon dioxide matrix,” *Nanotechnology*, vol. 19, no. 42, p. 424019, 2008.
- [27] S. H. Ng, J. Wang, D. Wexler, S. Y. Chew, and H. K. Liu, “Amorphous carbon-coated silicon nanocomposites: a low-temperature synthesis via spray pyrolysis and their application as high-capacity anodes for lithium-ion batteries,” *Journal of Physical Chemistry C*, vol. 111, no. 29, pp. 11131–11138, 2007.
- [28] Y. Chen, Y. Lin, N. Du, Y. Zhang, H. Zhang, and D. Yang, “A critical SiO_x layer on Si porous structures to construct highly-reversible anode materials for lithium-ion batteries,” *Chemical Communications*, vol. 53, no. 45, pp. 6101–6104, 2017.
- [29] W. Wu, J. Shi, Y. Liang, F. Liu, Y. Peng, and H. Yang, “A low-cost and advanced SiO_x-C composite with hierarchical structure as an anode material for lithium-ion batteries,” *Physical Chemistry Chemical Physics*, vol. 17, no. 20, pp. 13451–13456, 2015.
- [30] E. Fathi, Y. Vygranenko, M. Vieira, and A. Sazonov, “Boron-doped nanocrystalline silicon thin films for solar cells,” *Applied Surface Science*, vol. 257, pp. 8901–8905, 2011.
- [31] F. de Santiago, A. Trejo, A. Miranda et al., “Carbon monoxide sensing properties of b-, al- and ga-doped Si nanowires,” *Nanotechnology*, vol. 29, no. 20, article 204001, 2018.
- [32] O. I. Shevaleevskiy, “Structural defects and electrical conductivity in nanocrystalline SiC:H films doped with boron and grown by photostimulated chemical-vapor deposition,” *Semiconductors*, vol. 39, no. 6, pp. 709–711, 2005.



Hindawi
Submit your manuscripts at
www.hindawi.com

